Insights into the interaction dynamics between volatile anesthetics and tubulin through computational molecular modelling

Original
Insights into the interaction dynamics between volatile anesthetics and tubulin through computational molecular modelling / Zizzi, Eric A.; Cavaglià, Marco; Tuszynski, JACEK ADAM; Deriu, Marco A.. - In: JOURNAL OF BIOMOLECULAR STRUCTURE AND DYNAMICS. - ISSN 1538-0254. - 40:16(2022), pp. 7324-7338. [10.1080/07391102.2021.1897044]

Publisher:
Taylor and Francis

Published
DOI:10.1080/07391102.2021.1897044

Insights into the Interaction Dynamics between Volatile Anesthetics and Tubulin through Computational Molecular Modelling

Eric A. Zizzi [1], Marco Cavaglià [1], Jack A. Tuszynski [1,2,*] and Marco A. Deriu [1]

[1] Department of Mechanical and Aerospace Engineering (DIMEAS), Politecnico di Torino, Turin, Italy;
[2] Department of Physics, University of Alberta, Edmonton, AB, Canada;
* Corresponding Author: jacek.tuszynski@polito.it

Abstract: General anesthetics, able to reversibly suppress all conscious brain activity, have baffled medical science for decades, and little is known about their exact molecular mechanism of action. Given the recent scientific interest in the exploration of microtubules as putative functional targets of anesthetics, and the involvement thereof in neurodegenerative disorders, the present work focuses on the investigation of the interaction between human tubulin and four volatile anesthetics: ethylene, desflurane, halothane and methoxyflurane. Interaction sites on different tubulin isotypes are predicted through docking, along with an estimate of the binding affinity ranking. The analysis is expanded by Molecular Dynamics simulations, where the dimers are allowed to freely interact with anesthetics in the surrounding medium. This allowed for the determination of interaction hotspots on tubulin dimers, which could be linked to different functional consequences on the microtubule architecture, and confirmed the weak, Van der Waals-type interaction, occurring within hydrophobic pockets on the dimer. Both docking and MD simulations highlighted significantly weaker interactions of ethylene, consistent with its far lower potency as a general anesthetic. Overall, simulations suggest a transient interaction between anesthetics and microtubules in general anesthesia, and contact probability analysis shows interaction strengths consistent with the potencies of the four compounds.

Keywords: Volatile Anesthetics; Molecular Dynamics; Molecular Docking; Tubulin; Microtubules, Cytoskeleton

List of Abbreviations:

COM	**Center of Mass**
MAC	**Minimum Alveolar Concentration**
MD	**Molecular Dynamics**
MT	**Microtubule**
RMSD	**Root-Mean-Square Deviation**
RMSF	**Root-Mean-Square Fluctuation**
VA	**Volatile Anesthetic**

---

1. Introduction

General anesthetics are a unique class of drugs in modern medicine. They are able to reversibly suspend conscious brain activity while sparing most of the other brain functions with extraordinary selectivity. This, along with their analgesic and amnesic properties, has effectively made them a cornerstone of modern surgery, yet little is known about their molecular mechanism of action. This issue encompasses a rather large subset of open questions at many different scales: research failed to determine a single biological site of action capable of explaining not only the clinical manifestation of general anesthetics, but also the lack of any anesthetic effects in certain molecules with similar physicochemical properties[1]. Theories of anesthetic action started from early considerations on their solubility in lipid-like media, pioneered by the Meyer-Overton correlation [2–4] which is shown in Supplementary Fig. S1, to subsequent studies regarding effects on hydrophobic, lipid regions of the brain cells' membranes. Most recently, after further studies highlighted significant involvement of cytoskeletal proteins based on post-anesthetic-exposure proteomic alterations [5–7], investigations focused on possible involvements of the cytoskeleton, specifically microtubules (MTs), in the processes of memory formation, consciousness and side effects of anesthesia.

The theory elaborated in the 1980s by Penrose and Hameroff proposed to explain consciousness as the result of quantum resonance in the microtubule bundles extending to a neuron and eventually an entire brain, and is referred to as the 'Orch OR' theory [8], later expanded to what is known as the Quantum Mobility theory [1], based on computational evidence of alterations in the oscillation frequencies of π-electrons in aromatic amino acids of microtubules in the presence of anesthetics, with possible long-term effects also on MT polymerization. While the Orch OR theory has not been confirmed experimentally yet, the binding of anesthetics to tubulin is known to occur experimentally [9], and interactions between the latter and anesthetic agents are of particular interest due to potential implications in (a) Post-operative cognitive dysfunction (POCD), which is associated with microtubule instability and the separation of microtubule-associated protein (MAP) tau from MTs [10,11]; (b) memory formation, a process relying on synaptic plasticity [12–14] which is impaired during general anesthesia and has been linked in previous computational studies to the microtubule lattice [15]; (c) the unique spatial organization of microtubules in neurons [16,17] and their putative ability to create specific conduction pathways, hypothesized to be involved in information processing [15,18–20]; (d) clinical decisions regarding anesthesia in patients undergoing chemotherapy or with neurodegenerative comorbidities, both of which can imply pathological or drug-induced alterations of the microtubule cytoskeleton respectively, which might be influenced by the simultaneous presence of anesthetics [21,22].

These considerations support the investigation of microtubules, and their constitutive protein tubulin, as a putative target for anesthetic molecule interactions.

Indeed, volatile anesthetics (VAs) exhibit many different chemical structures and cover a wide range of molecular weights, from single atoms such as Xenon to heavier halogen-substituted ethers such as Sevoflurane. Among these, Halothane (2-bromo-2-chloro- 1,1,1-trifluoroethane) is a volatile haloalkane with a MAC of 0.74% [23]. Experimentally, it has been found to alter the genetic expression of tubulin [6] and to directly bind to it [9]. Also, it is known to alter the polymerization rate of tubulin in microtubules in vivo [24,25], and thus is of particular interest in the context of VA-tubulin interaction. Conversely, Desflurane (2-(difluoromethoxy)-1,1,1,2-tetrafluoroethane) is a poorly soluble, fluorinated ether with a slightly higher MAC value of 6% in oxygen [26], also causing alterations in tubulin expression after exposure *in vivo* [5]. Methoxyflurane (2,2-dichloro-1,1-difluoro-1-methoxyethane) is a potent anesthetic gas, also belonging to the class of halogenated methyl ethyl ethers, with a MAC value of just 0.16% [27], and now mostly abandoned as a general anesthetic due to the nephrotoxicity of its metabolites [28]. It has been shown, just as Halothane, to influence the polymerization of tubulin *in vitro* and significantly alter the axonal microtubule structure [29]. Lastly, ethylene (or ethene) is the simplest alkene and has a comparably low molecular weight of just 28.054 g/mol. It is highly volatile and with a MAC value of as much as 67% [30], but it is not used as a general anesthetic due to its very low potency.

The four above-mentioned VAs were chosen for our investigation not only due to experimental evidence of interaction with tubulin, but also to cover a wide range of clinical potencies (MAC values of 0.16% for Methoxyflurane up to 67% for ethylene), and to include molecules belonging to different classes (namely, ethers, alkanes and gases as classified in [26]).

To investigate the effect of said anesthetics on the cytoskeleton network, in the present work tools provided by Computational Molecular Modeling, namely Homology Modelling, Molecular Dynamics and Molecular Docking were deployed to provide new insights into their interaction at an atomic scale as those tools have widely demonstrated their value in investigating the molecular basis of biological effects [31–38].

2. Materials and Methods

2.1. Homology Modelling of human tubulin isotypes

Due to the lack of experimentally determined 3D structures for most human tubulin isotypes, αβ-tubulin dimers were modeled according to previous tubulin modelling protocols based on crystallographic data for bovine and porcine tubulin [39,40]. Following the nomenclature also found in Leandro-García et al. (2010) [41], human isotypes βVI (Beta-1, Class VI, Gene TUBB1), βIIa (Beta 2A, Gene TUBB2A) and βIVa (Beta 4A, Gene TUBB4) were chosen for this analysis; βIVa and βIIa were chosen due to their highest reported expression in the brain tissue with respect to other tubulin isotypes (46% and 30%, respectively); βVI was chosen as a non-brain-specific control [41]. Manually annotated and reviewed amino acid sequences for human tubulin isotypes αIa, βVI, βIIa and βIVa were downloaded from the UniProt database (accession codes Q71U36, Q9H4B7, Q13885 and P04350, respectively). Since the goal was to model human tubulin in its dimeric form, the 3J6F [42] entry from the Protein Data Bank (www.rcsb.org) was selected as a template, consisting of a minimized structure of GDP-bound microtubules with a resolution of 4.9 Å. First, the alpha and beta tubulin isotypes were modeled as single monomers. To do so, sequence alignment to the 3J6F target was carried out using UCSF Chimera software [43] and missing residues were modelled using modeller 9.21 [44]. Then, the homology model was built using modeller 9.21 with the options of building models with hydrogens, using thorough optimization and performing loop refinement. All models were built including their C-terminal domains. The generated models were evaluated based on the GA341 and zDOPE score, inspected manually by visual comparison to the target structure, and further checked using the packages PROCHECK [45], WHATCHECK [46], ERRAT [47] and Verify-3D [48]. A further quality assessment was carried out using the QMEAN score [49,50] implemented in the SWISS-MODEL server [51]. The same general protocol was subsequently used to generate αIa-β-tubulin dimers for every β isotype mentioned, since data regarding β tubulin isotype expression is readily available in the literature and the present interaction study was also aimed at assessing differences between β tubulin isotypes.

2.2. Molecular Docking

To evaluate putative binding sites for anesthetic molecules of interest, conformations for each tubulin dimer were extracted every 10 ns from the second halves of each of three 100ns MD simulations of the tubulin dimer with each VA and exported in pdb format, yielding 18 protein snaphots for each of the three dimers, each simulated with one of the four anesthetics, for a total of 18 snapshots * 3 isotypes * 4 anesthetics = 216 protein snapshots. AutodockTools [52] was subsequently used to add Gasteiger charges information and export the snapshots in pdbqt format. The 4 anesthetics were obtained in 3D-SDF format from the DrugBank database (www.drugbank.ca) , energy minimized with explicit hydrogens and exported in pdbqt in AutodockTools, again assigning Gasteiger charges. Docking was performed in AutoDock-Vina [53], which accounts for ligand flexibility by continuously rotating rigid parts of the ligands around rotatable bonds and keeping the protein rigid. The search box, centered at the center of mass (COM) of the dimer was built in order to encompass the whole dimer and perform blind docking, and the center of the search box was conserved at the COM of the dimer in all blind docking runs, for all anesthetics. For all docking runs, the exhaustiveness was set to of 64 and the maximum number of binding modes to be generated was left at the program's default setting of 9 poses per run, providing a good compromise between speed and pose sampling. With 9 conformations generated in each docking run, repeated for a total of 216 protein snapshots as discussed above, a total of 9*216=1944 docked conformations were generated, 162 for each anesthetic-isotype pair. Considering the low affinity difference between predicted poses, around tenths of kcal/mol, all of these 162 docking poses were analyzed for each ligand-isotype blind docking run. To facilitate the analysis and comparison of individual docking results, said 162 binding poses obtained from blind docking for each isotype-VA pair were exported in pdb format with the dimer, and residues within 6 Å of the ligand were extracted using GROMACS, and saved along with the corresponding predicted affinity of the pose into a simple text file. A custom MATLAB code was subsequently deployed to count the occurrence of each residue across all the 162 poses of each docking run, and the 50 most recurring residues were deemed as involved in binding sites with the highest consensus, given the negligible difference in affinity among different docking poses, below the noise level of k_BT, and further analyzed. The predicted binding affinity of each anesthetic for each tubulin dimer is also reported, as mean ± standard deviation of all output poses.

To check and refine the above-described blind docking approach, a local docking validation has been carried out as exhaustively explained in the Supplementary Information.

2.3. Molecular Dynamics

For molecular dynamics simulations tubulin isotypes βVI, βIIa, βIVa were chosen for investigation, each in its dimeric form with αIa tubulin. Each dimer was completed with GTP, GDP and the Mg^{2+} ion from the 3J6F template, and each was simulated both without anesthetics, and separately with halothane, desflurane, methoxyflurane and ethylene present in the surrounding solvent at a concentration of 10 mM, which experimentally showed polymerization inhibition of microtubules [54] and is at the upper end of the range of clinical concentrations for more potent volatile anesthetics. It is to be noted that data regarding intracellular concentration of volatile anesthetics during general anesthesia is fairly dispersed, reporting concentrations ranging from a few mM[55] up to hundreds of mM [56], possibly due to the large differences in potency between different compounds. Overall, a total of 15 systems for Molecular Dynamics simulations were obtained – 3 isotypes times 4 anesthetics + control without anesthetics– and each was simulated in three replicates by re-initializing velocities from the Maxwell distribution at 300K at the beginning of the NVT equilibration. The Visual Molecular Dynamics [57] (VMD) environment was used for visual inspection of the systems and trajectories and for further roto-translational corrections. GROMACS 2019.1 [58] was used for MD simulations, specifically with the AMBER ff99SB-ILDN force field [59]. Molecular 3D structures for the 4 volatile anesthetics were obtained in 3D-SDF format from DrugBank [60], energy minimized with explicit hydrogens, and their topologies, just as for GTP and GDP, were generated through the ANTECHAMBER [61] package employing the AM1-BCC charge method [62] and the general AMBER force field. The MD system was configured in GROMACS in a dodecahedral box with xyz periodic boundary conditions and a minimum distance between the protein and the box edge of 1.0 nm, to avoid interaction with periodic images. All the systems were solvated with TIP3P explicit water and neutralized with counterions. Moreover, a physiological ionic strength of 0.1 M was imposed by adding appropriate amounts of Na+ and Cl- ions. In the case of systems with anesthetics, a custom script was deployed to add an appropriate number of molecules given the target concentration of 10 mM. The minimization was carried out using the steepest descent method, with 1000 kJ/(mol*nm) maximum force and no restriction on maximum steps. All subsequent steps, namely equilibration in NVT and NPT ensembles along with the production NPT simulations were carried out remotely on HPC resources. The NVT and NPT equilibrations were carried out at T=300K and P=1.0 bar, respectively, with the protein restrained and a total of 100 ps each. In the case of NVT, the modified Berendsen thermostat[63] was used with τ constant of 0.1, while NPT equilibration was carried out using the Parrinello-Rahman barostat [64] with isotropic coupling and a τ constant of 2.0. For both NVT and NPT equilibrations, PME [65] Electrostatics were used, with an interpolation order of 4 and an FFT grid spacing of 0.16 nm. Production simulation followed in the NPT ensemble, without any restraint, for 100 ns per replica with a 2 fs timestep and coordinate saving set every 1000 steps, i.e. every 2 ps. The stability of the tubulin dimer during the simulation was determined by the RMSD of the protein backbone followed by cluster analysis, both carried out in GROMACS.

2.4. Analysis

2.4.1. Structural Effects

The structural effects on the dimer in the presence of the VAs were evaluated by analyzing the RMSF with and without anesthetic molecules, as calculated with GROMACS excluding the highly fluctuating C-terminal regions, and separately for the alpha and beta subunit of the dimer. Structural effects were further assessed using cluster analysis on each simulation, as implemented in the gmx cluser tool of GROMACS, using the single linkage method with 0.15 nm RMSD cutoff. Effects on secondary structure were assessed using DSSP 3.0.0 [66] after extracting snapshots every 100 ps from the last 50 ns of each simulation.

2.4.2. Contact Probability

To quantitively assess the interaction between each of the four anesthetics and the tubulin dimer, the raw trajectory was analyzed: for each frame, the minimum distance between each residue and any ligand molecule in the solvent was calculated with GROMACS. A custom script subsequently calculated the per-residue contact probability by averaging interactions in each frame between residues and ligands. Following previous computational work [38], the ligand was considered to be in close contact with a residue whenever its distance to that residue fell below 2.8 Å, corresponding roughly to the diameter of a water molecule, and at the end the overall probability of contact with the anesthetic was obtained for each residue over the whole trajectory consisting of the concatenation of the last 50 ns of each of the 3 replicates. The individual contribution of the second half (50ns) of each replica of a given system to the per-residue contact probability was also calculated and is reported in the Supplementary Information. Residence times of each contact event were calculated by counting the number of consecutive frames in which the ligand stayed within 5 Å of a given residue. This cutoff was chosen to include consecutive frames in which the ligand briefly repositions itself, temporarily increasing its distance to the residue above the 2.8 Å cutoff used for contact probability calculation, but effectively staying in the same binding pocket. To efficiently compare contact areas between different isotypes and different anesthetics, the system was analyzed in a spherical coordinate system, built as follows: the position of each dimer was aligned with a custom VMD script so that the origin of the cartesian coordinate system relocated to the center of mass of the dimer, between the alpha and beta subunit: this way, residues belonging to the alpha subunit had coordinate $z > 0$, residues on the beta subunit had $z < 0$ and residues at the alpha-beta interface had $z \cong 0$. Subsequently, another custom VMD script rotated the dimer so that the x axis was parallel to the vector connecting the Cα of residues α128Q and α285Q, which are known to be involved in lateral contacts between adjacent protofilaments [67]. This allowed to broadly discriminate between residues located towards the abluminal side of the microtubule, residues located towards the luminal side and residues involved in lateral contacts, based on their y coordinate ($y > 0$ corresponds to residues facing the outer surface of the MT, $y < 0$ residues facing the lumen and $y \cong 0$ residues involved in lateral contacts between adjacent protofilaments), as highlighted in Figure 1.

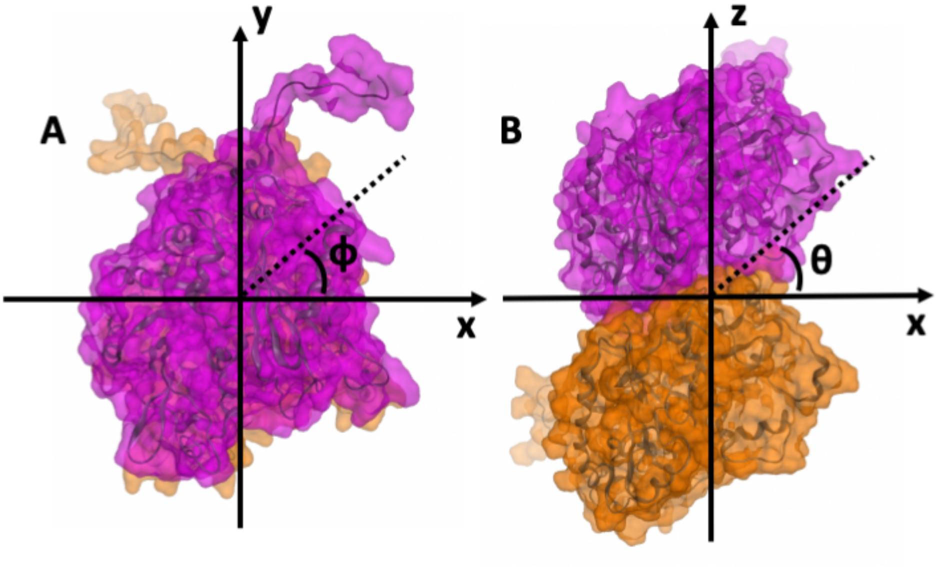

Figure 1. (**a**) Schematic representation of the phi angle from a top view of the tubulin dimer, which represents the azimuthal position in the xy plane, around the z axis: positive values correspond to the outer side of the protofilament while negative values correspond to the inner side; (**b**) Schematic representation of the theta angle from a side view of the tubulin dimer. Elevation theta represents the angular position between the z axis and the xy plane: negative values correspond to the beta subunit (shown in orange), while positive angles represent residues on the alpha subunit (shown in pink).

To better represent and interpret the data, the geometrical center of each residue was determined using the MDAnalysis[68,69] toolbox for python, and its (x,y,z) Cartesian coordinates subsequently transformed into spherical coordinates with an *ad-hoc* python script. In this new system, the elevation angle theta was calculated starting from the xy-plane, so that $\theta > 0$ corresponds to points with $z > 0$ and vice versa. The φ angle on the other hand represents the azimuth, i.e. the rotation around the original z axis. A 3D rendering of the tubulin dimer in this new spherical coordinate system is shown in Supplementary Video S1. Residues were represented in this new coordinate system, with the radial coordinate ignored. As a matter of fact, since contact in the 100ns trajectories only occurs on the surface, there is no chance of radial ambiguity and a single couple of (θ, φ) always identifies a single surface residue in this spherical approximation, except for the highly fluctuating C-terminus, which was checked for contact by visual inspection of the trajectories. To further enhance this representation, the surface on the tubulin dimer has been divided into sectors on the theta-phi plane. Instead of plotting the contact probability of individual residues, the contact probability was evaluated on a per-sector basis: contact was recorded on a given sector of the dimer surface in a frame of the MD trajectory if any of the residues within that sector were within 2.8 Å of any anesthetic molecule. Contact counts were subsequently normalized to the total number of frames to yield the contact probability. The resulting coordinate system, as previously discussed, implies that the four quadrants qualitatively represent distinct areas on the dimer, as reported in Table 1.

Table 1. Quadrants on the (theta,phi) plane and corresponding gross locations on the dimer.

Quadrant	θ	φ	Subunit	MT surface
I	> 0	> 0	Alpha	Abluminal
II	< 0	> 0	Beta	Abluminal
III	< 0	< 0	Beta	Luminal
IV	> 0	< 0	Alpha	Luminal

After qualitatively assessing the location of highly interacting residue groups in this representation and checking for recurring interaction patterns across different anesthetics and different tubulin isotypes, each trajectory was further analyzed manually, and the regions of interaction inspected and reported. The main binding clefts where interaction consistently occurred across different replicas (corresponding to dark areas on the contact probability maps) were precisely defined – in terms of residues forming the clefts – and reported. Their location is also reported in the previously mentioned coordinate system to aid their visual localization on the dimer and allow for a direct comparison with overall contact probabilities.

To statistically assess whether the differences in per-residue contact probability between the four tested ligands for a given isotype were significant, a one-way ANOVA was used, testing the null hypothesis that the means of the contact probabilities for each group (i.e. with each of the four ligands) are equal, rejected at $p<0.05$. This allowed to determine if at least one of the ligands had a significantly different probability of interacting with the tubulin dimer. To further compare the contact probabilities of Ethylene, the weakest molecule used as a control reference, versus the contact probabilities of the other three ligands (Desflurane, Halothane and Methoxyflurane), Dunnett's Test was used with a significance threshold of $p<0.05$.

2.5. MM/PBSA Binding Energy estimation

To provide a further quantitative assessment of the interaction between the four simulated anesthetics and the tubulin dimer, MM/PBSA [70] estimations of binding energies were performed for all four tested anesthetics. More in detail, for each of the four anesthetics, the following workflow was adopted: starting from the contact maps obtained from the MD simulations with anesthetics, the main binding clefts were identified as described above. Subsequently, the concatenated trajectories containing the last 50 ns at equilibrium of each of the three replicas, from which the contact probability maps were built as described previously, were iteratively filtered for frames where the given anesthetic was present in the cleft. This was repeated for all anesthetics and for all clefts, so that sub-trajectories were generated for each ligand and each cleft, representing different snapshots of the bound state. These trajectories were used for MM/PBSA calculations using the *pbsa* tools included in AmberTools 20 [71], after converting GROMACS trajectories and topologies into their respective amber counterparts using ParmEd. Calculations were performed using one every two frames. The final binding affinity and the contributions of the VDWAALS, EEL, ENPOLAR and EDISPER components are also reported on the same, sectorized (θ,φ) plots as the contact probability maps, to provide a direct comparison and a visual localization of the different clefts.

2.6. Plots and Figures

Data plots for RMSD and RMSF distributions were generated using the Grace package. Three-dimensional representations of the tubulin dimers were rendered in VMD and in MOE, while auxiliary figures for the spherical coordinate system were assembled in Microsoft PowerPoint. The animated 3D-view of the tubulin dimer within its spherical coordinate system, with the theta and phi angles highlighted, was generated using a 3D rendering of the dimer in Blender 2.80 and is available in the Supplementary Information. Sectorized contact probability plots, residue count histograms from docking runs and MM/PBSA binding energy maps and their corresponding decomposition maps were generated in MATLAB. Detailed, 3D views of docking pose ensembles and of interesting MD contact sites on the dimer and Ramachandran plots reported in Supplementary Figure S2 were generated in MOE 2019.01 [72].

3. Results

3.1. Homology Modelling

Modeller 9.21 [73] was used to build homology models for human isotpyes βVI, βIIa and βIVa in dimeric for with α1a tubulin, starting from the 3J6F PDB template. The four modeled sequences αIa, βVI, βIIa and βIVa shared an identity with the respective 3J6F templates of 99.32% (sequence Q71U36), 80.80% (sequence Q9H4B7), 99.06% (sequence Q13885) and 97.19% (sequence P04350) respectively. The obtained models all showed comparable zDOPE scores fluctuating around -1.55 ± 0.1 for β tubulin and -1.49 for the α1a isotype. PROCHECK [45] validation reported more than 94% of residues in most favoured regions and no residue in disallowed regions for every isotype modeled. QMEAN4 values for the three modelled α-β dimers were -1.56 for αβVI, -1.49 for αβIIa and -1.67 for αβIVa, respectively, while the 3J6F template dimer had a QMEAN4 value of -0.37. The quality of the models was confirmed through the tools Verify-3D [48], WHAT_CHECK [46] and ERRAT [47] as shown in detail in the Supplementary Material.

3.2. Docking

Firstly, blind docking was performed for all isotypes with all anesthetics by setting the grid box geometry so as to encompass the whole dimer, centered at the COM of the latter. Across all the 162 blind docking poses determined for each anesthetic-isotype pair, the average predicted binding affinities are shown in Table 2. Data points are reported in kcal/mol, as mean ± standard deviation.

Table 2. Predicted binding affinities in kcal/mol with each anesthetic, reported as mean and standard deviation calculated among the 162 docking poses for each isotype-anesthetic pair.

	Isotype		
	αβVI (kcal/mol)	**αβIIa (kcal/mol)**	**αβIVa (kcal/mol)**
Ethylene	-2.00 ± 0.14	-2.00 ± 0.16	-2.01 ± 0.15
Desflurane	-5.15 ± 0.24	-5.02 ± 0.22	-5.02 ± 0.23
Halothane	-4.45 ± 0.26	-4.14 ± 0.17	-4.45 ± 0.34
Methoxyflurane	-4.22 ± 0.18	-4.26 ± 0.30	-4.25 ± 0.26

Overall, blind docking yielded binding affinity ranges consistent with combinations of hydrophobic Van der Waals-type interactions. Ethylene consistently showed very low affinity values hovering around -2.00 kcal/mol with little differences among different poses on the same snapshot and among different snapshots of the same isotype (as seen by the comparatively low std. dev.), along with little differences between isotypes. The differences in affinity between the other three ligands were more subdued, and with a slightly higher std. dev., highlighting how some docking poses and sites were predicted to be more energetically favorable for hosting these molecules with respect to others. Overall, Desflurane reported the best predicted affinity across all three isotypes, while the predicted affinities for Halothane and Methoxyflurane were comparable.

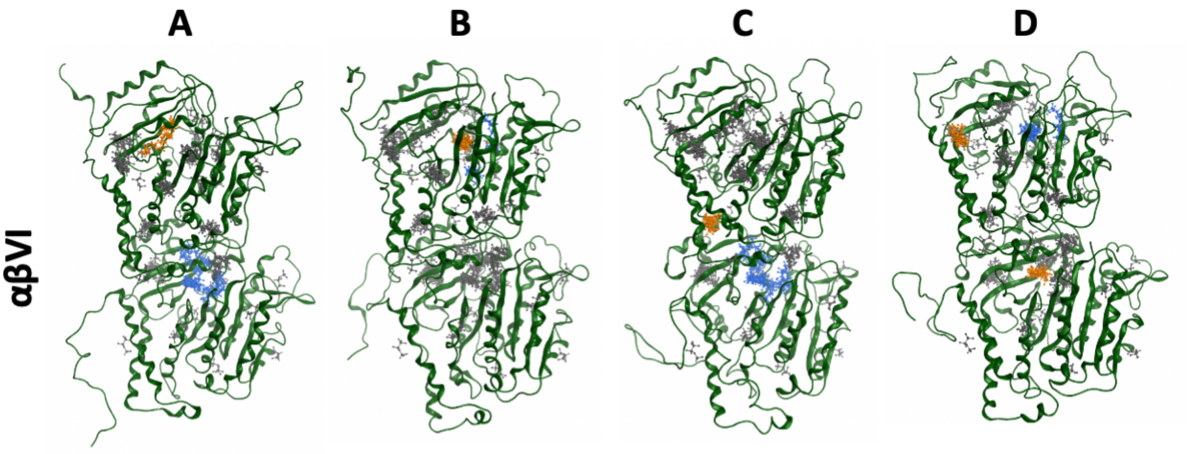

Figure 2. Ensemble of docking poses on the αβVI dimer, with individual poses shown in grey: (**a**) Desflurane; (**b**) Halothane; (**c**) Methoxyflurane and (**d**) Ethylene. The largest clusters of recurring

poses are highlighted in blue, clusters of poses with highest average predicted binding affinity (most negative) are highlighted in orange.

In terms of binding sites, isotype αβVI (shown in Figure 2) featured with Desflurane a large number of docking poses around βILE368, βLEU250, βALA314, βILE236, βLEU253 and βASP249, while the binding site with highest predicted affinity was located around αPHE202, αALA201 and αMET203. In the case of Halothane, the most frequently involved residues were αTRP21, αALA65, αPRO63, αGLY17, αPHE67, with the best overall affinity at the sites around αGLU168, αVAL137, αLEU167 and αPHE202. Methoxyflurane consistently docked as Desflurane near βLYS252, βLEU253, βALA254, βALA314, βASP249, βMET257, βILE316, βASN247, an area delimited at the top by αASN101 at the inter-monomer interface, with peaks of highest affinity around βARG251, αALA99 and αSER178. Ethylene did not show specific preferred binding sites, but docked with slightly more frequency around αPHE138, αVAL235 and αPHE169, with best affinities at the sites around βILE368 and αTRP388. In the case of isotype αβIIa with Desflurane, the most recurring sites were two, located between αTYR172, αSER187, αHIS139, αSER140, αSER170, and αPHE141, with one of them, involving also αTHR190 and αTHR191, αGLU168, and αTHR194 also showing the lowest average affinity across the poses. With Halothane, the frequent locations were at βARG251, αPHE141, αSER187 and αPRO173, with low-energy sites around αLEU92, αILE122, αALA65, αARG121, αGLU90, αGLN91, αPRO63, αVAL62 and αVAL66. Methoxyflurane frequently docked at αPHE141, αSER147, αTHR194, αGLY142, αTHR190 and αTHR191, with the highest affinities predicted around βPHE294, βTYR310 and βVAL313, βMET293. Ethylene again was not predicted to have preferred sites, with a slightly higher count of poses around αTRP388, αMET203, αPHE267, αALA201 and αPHE202, αPRO173. A lower-energy binding site was predicted around βPHE294, also found in the previous case. Lastly, docking of Desflurane to isotype αβIVa predicted three recurring binding sites around αILE384, between βVAL236, βTHR237 and βGLU198, and near αTHR239 and αLEU136 respectively, with the latter also with comparatively high affinity across the different sampled poses, especially in poses in close contact with αPHE138 or αPHE135. Halothane frequently docked into a cleft lined by αLEU92, αPHE67, αGLN91, αVAL14, αVAL78, αPHE87 and αASN18. The binding site with lowest average binding energy was instead located between βVAL333, βGLN334, βMET330 and βVAL349. Docking of Methoxyflurane frequently accommodated the ligand in a cleft lined by βALA248, βASP249, βLEU240, βLEU253, βLYS252, βASN247, βLEU250 and βILE368, which was also predicted in [54], with high-affinity sites located instead surrounded by αGLY81, αPHE67, αPHE87, αTHR82, αTYR83, αVAL78 and αARG84. Lastly, ethylene frequently docked into a broader area delimited by αTRP21, αHIS8, αPHE67, αTYR24, αGLY17 and αVAL235. Poses near αHIS8 were also the ones with lowest mean energy, along with poses docked to a second site near αTHR150. For a graphical summary of frequently found residues across all docking poses, along with the mean predicted affinity associated with the respective poses, see supplementary information.

To check and further refine the ligand-protein binding estimation, a second set of local docking runs was performed, which confirmed data and trends reported from blind docking (see Supplementary Information and Supplementary Table ST1).

Overall, the binding sites found by docking were generally lined by a majority of hydrophobic residues, which again suggests a predominantly hydrophobic interaction, consistent with the predicted affinity estimates. In blind docking, isotype αβVI showed putative interactions on both subunits, isotype αβIIa had more overall binding poses on the alpha subunit, and isotype βIVa showed a similar number of binding poses on both subunits. The results from blind docking, and their subsequent validation through local docking refinement, confirmed the main drawbacks of docking techniques in the context of ligands interacting with low affinity, possibly within multiple, energetically equivalent binding sites on the dimer simultaneously. This level of investigation is not accessible to plain docking. Overall, the lack of an experimentally known set of binding sites against which to perform docking, along with the mentioned methodological drawbacks such as the inaccuracy of predicted affinity[74], especially in the context of the systems under investigation in the present work, justified a more detailed analysis of the sites of interaction through the use of Molecular Dynamics, in the light of the low interaction strength and absence of evidence for a specific, 'lock-and-key'-type binding site for anesthetics. Indeed, the adopted molecular dynamics approach allows for a more efficient sampling of multiple, simultaneous, low-affinity binding sites on the dimer surface, by simulating the dimer with a fixed anesthetic concentration in the solvent. This enables the statistical investigation of the most explored areas, which is not feasible through docking alone.

3.3. Protein Ligand binding dynamics

3.3.1 Molecular Dynamics stability analysis

First, the stability of all the simulations was checked by examining the RMSD over each 100ns trajectory. All three isotypes had reached a plateau after about 50 ns, with the αβIVa dimer in the presence of Desflurane being the only case with slightly more accentuated fluctuations up to about 70 ns. See Supplementary Figure S3 for the complete RMSD details. Potential energy plots for all simulated systems are reported in Supplementary Figure S4.

3.3.2 Protein-Ligand interaction dynamics

Molecular Dynamics simulations allow to overcome the limitations of the docking approach in the context of low-affinity ligands, such as the volatile anesthetics investigated in the present work, which interact simultaneously in multiple sites on the tubulin dimer. Simulating the dimers in the presence of VAs in the surrounding solvent at a fixed concentration enables a more significant sampling of frequent interaction clefts, including simultaneous interaction in multiple, low-affinity binding sites, and provides a quantitative assessment thereof, which is precluded to single-ligand docking in the case of weak binding events.

Per-residue contact probabilities extracted from MD simulations show preferential interaction with specific residues for each anesthetic and for each isotype. The contact probability plots, reported in the Supplementary Information, visually highlight how the different anesthetics interact with partially different strengths and in specific locations, both on the same tubulin isotype and across different isotypes, albeit some commonly involved residues emerge. Ethylene clearly displays lower overall contact probabilities, in a manner consistent both with its considerably lower potency in clinic and with the significantly lower predicted affinities in blind and local docking runs. To better highlight the actual location where binding occurs, both longitudinally along the major axis of the dimer (i.e. *on which subunit and how far from the inter-monomer interface*), and circumferentially around said axis (i.e. *where around the dimer*), the contact probabilities are reported on a sectorized spherical coordinate system in terms of theta and phi angles, where elevation theta discriminates between subunits and azimuth phi locates residues around the dimer (see details described in the Methods section). Such contact maps highlight the patterns of interaction between each anesthetic and specific tubulin isotypes and provide qualitative information about preferential binding location both around the dimer (luminal vs. abluminal side in the MT) and longitudinally along the major axis (top α-subunit vs. α-β interface vs. bottom β-subunit). The resulting high-probability contact areas are shown in Figure 4 for the most highly interacting isotype, namely αβIVa, which is also the most highly expressed in the brain.

To visualize the proximity of tryptophan residues, which is a key requirement of the Quantum Mobility theory of anesthetic action [18], also in comparison to previous computational work [1] predicting aromatic amino acids as functional targets of anesthetics on tubulin, the location of Trp residues on the tubulin dimer in this spherical coordinate representation is shown as orange crosses on the heatmaps in Supplementary Figure S6.

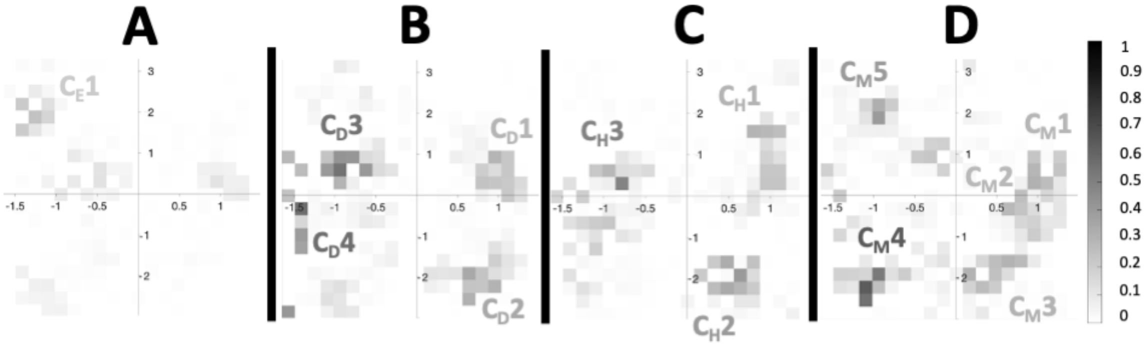

Figure 3. Per-area contact probability for isotype αβIVa, the one with the most overall interactions, with all the tested ligands. (**a**) Ethylene; (**b**) Desflurane; (**c**) Halothane and (**d**) Methoxyflurane. Color scale is 0 to 1, i.e. 0% to 100% probability of interaction with any residue within a given area. The main recurring interaction clefts are also highlighted, with the subscript differentiating the four ligands.

Briefly, Desflurane interacts substantially on the β subunit of isotype αβVI, both on the luminal and abluminal side of the dimer, along with different inter-monomer transient contact clefts. A distinct interaction zone also emerges on subunit alpha laterally (where φ is close to 0), enclosed by residues α293ASN on helix αH9 and α334THR on helix αH10. On isotype αβIIa, interaction was recurring more markedly on the α subunit mainly at the same lateral contact area already seen in the previous case between H9 and H10. Minor contact probabilities were also recorded on the luminal side of the alpha subunit, and on the abluminal and lateral area of subunit beta. The interaction is similar on isotype αβIVa (Figure 3B), with a high probability of residence laterally between H9 and H10 subunit alpha, with the addition of recurring interaction on the β subunit, laterally in close proximity to the exchangeable GTP binding site, between helix H6 and the start of H7, near residues β208TYR, β221THR and β225LEU, and transiently on the rest of the surface. Halothane showed slightly lower overall contact probabilities, especially on isotype αβIIa. A high probability of residence is again visible on the α subunit's H9-H10 lateral contact zone on all three simulated isotypes. Interaction sites were more abundant on isotype βIVa (Figure 3C), a substantial fraction of which on the luminal side of the dimer, with two distinct clusters on the α and β subunit and the addition of an interaction site on the lateral contact area of the β subunit, a semi-closed cleft defined by residues β231ALA and β227HIS belonging to helix H7 and capped by the sidechain of β276ARG of loop S7-H9 which folds over the ligand molecules (up to two halothane molecules at the same time seen during the simulation). Methoxyflurane, the most potent anesthetic – i.e. the one with the lowest MAC – showed the highest number of high-probability contact sites for all three simulated isotypes, with the addition of the highest overall residence times (and thus contact probabilities). Interaction was ubiquitous on isotype αβVI, with contacting residues localized on both subunits and on either side, luminal and abluminal. Isotype αβIIa showed mostly overlapping areas of preferential residence. The interaction with isotype αβIVa (Figure 4D) was recorded both on the luminal and abluminal sides of both the α and β subunit. Notably, this isotype showed a unique interaction area located on the luminal side of the beta subunit, in a binding site near βGLY79 at the end of helix H2. The lateral contact area towards the top of the α subunit was again involved in numerous contacts with methoxyflurane on all three isotypes.

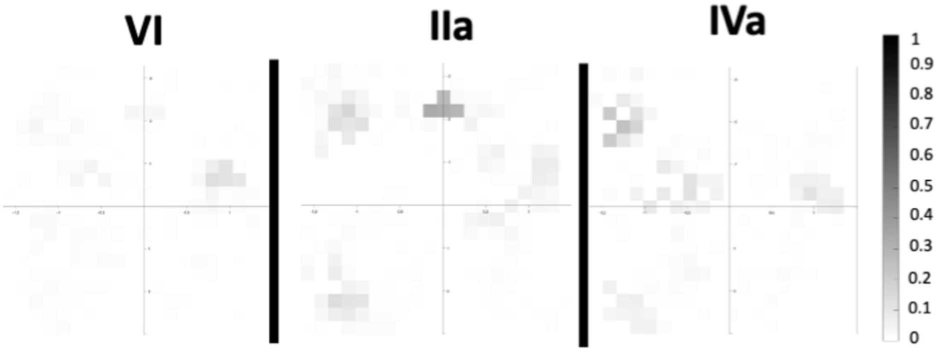

Figure 4. Contact probabilities of Ethylene with all three simulated isotypes (left to right: αβVI, αβIIa, αβIVa), which is visibly lower than the amount of contact of the other three anesthetics.

Ethylene (Figure 4) showed a much weaker overall interaction with the tubulin dimer, visible both during the simulations themselves and on the contact probability analysis. With the exception of a more frequent interaction on isotype αβIIa, on the abluminal site of the α-β inter-monomer interface (a cleft between H11 and H12, on H11′, lined by residues β413MET, β415GLU, β409VAL, β418PHE and β408TYR), residence on the surface of the dimer was transient and with very low overall probability, demonstrating how the ligand spends most of the simulation time floating freely in the solvent. This is consistent not only with the significantly lower predicted affinities through docking and low molecular weight of the molecule, but also with the much lower efficacy as a volatile anesthetic if compared to the other compounds.

In summary, the analysis of the described interaction hotspots, i.e. the areas with highest contact probabilities visible as dark zones in Figures 3 and 4, pinpoints the location of specific transient binding clefts. These were characterized in detail, and are marked in Figure 3, numbered progressively and with the subscript indicating the involved anesthetic. The detailed description of the main binding clefts, with their adopted nomenclature and the list of involved residues, is provided in the following Table 3 for isotype αβIVa. The corresponding table for isotypes αβVI and αβIIa is provided in the Supplementary Information.

Table 3. Binding clefts for isotype αβIVa for all the simulated anesthetics.

Ligand	Cleft	Residues
Desflurane	**C_D1**	αILE335, αLYS336, αILE332, αASN329, αVAL328, αPRO325, αGLY350, αPHE351, αVAL353, αILE355
	C_D2	αGLU90, αGLN91, αPRO89, αLEU125, αLYS124
	C_D3	βARG306, βPRO305, βPHE294, βASN295, βALA296, βASN337, βSER339
	C_D4	βASN204, βGLU205, βTYR208, βVAL175, βTHR221, βTYR222, βPRO220
Halothane	**C_H1**	αILE335, αLYS336, αILE332, αASN329, αVAL328, αPRO325, αGLY350, αPHE351, αVAL353, αILE355
	C_H2	αGLU90, αGLN91, αPRO89, αLEU125, αLYS124, αILE75, αVAL78, αARG79, αARG84
	C_H3	βARG306, βPRO305, βPHE294, βASN295, βALA296, βASN337, βSER339
Methoxy-flurane	**C_M1**	αILE335, αLYS336, αILE332, αASN329, αVAL328, αPRO325, αGLY350, αPHE351, αVAL353, αILE355
	C_M2	αSER287, αGLU290, αALA294, αILE276, αLYS280, αALA281, αGLU284
	C_M3	αTHR82, αTYR83, αARG84, αARG79, αPHE87
	C_M4	βASP74, βGLY71, βPRO70, βPRO87, βASN89, βPHE90, βVAL91, βMET73, βVAL76
	C_M5	βARG390, βPHE389, βMET415, βASN414, βASP417
Ethylene	**C_E1**	βPRO182, βALA185, βVAL170, βSER168, βSER188, βVAL189

The interaction sites are distinct with each anesthetic but with notable overlaps, the most important of which is a vast binding area located on the upper part of the α subunit in the lateral PF-PF contact zone, and comprising clefts CD1, CH1 and CM1 in all isotypes and CM2 (isotype αβIVa and αβVI) and CD2 (isotype αβVI). Every anesthetic, except ethylene, stuck to a cleft in this area for a significant portion of the simulation, on all three isotypes. As discussed, this cleft is in fact formed by two distinct hydrophobic patches located at the proximity of helices H9 and H10, respectively, the latter located towards the top of the alpha subunit, thus actually on the longitudinal dimer-dimer interface. The first area, corresponding to clefts C1 and shown in Figure 5A, largely consists of a hydrophobic patch delimited on the lower part by the start of the S7-H9 loop and the final residues of S7, and on the upper part by helix H9 and the last residues of the S7-H9 loop, able to accommodate lipophilic ligands.

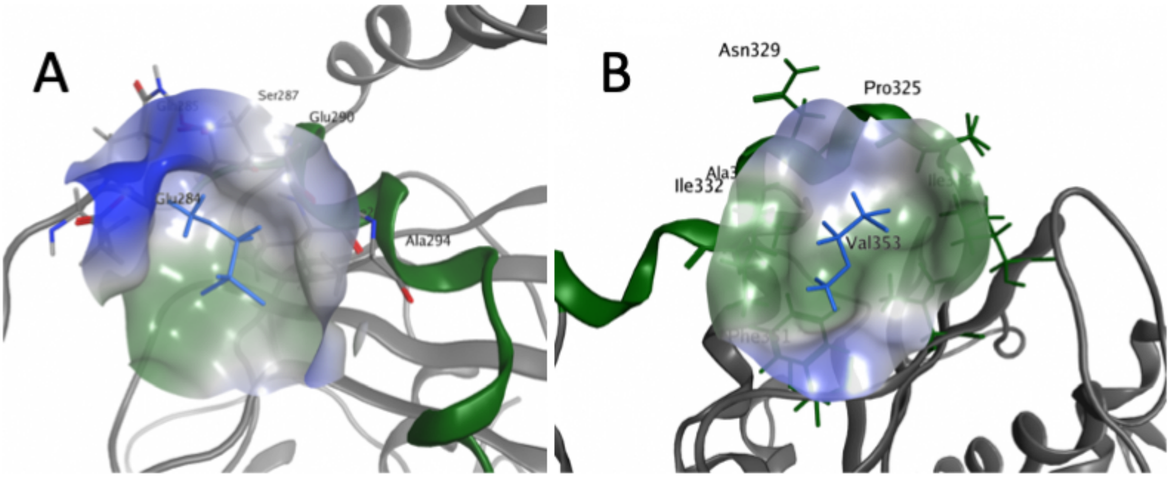

Figure 5. Rendering of the two sites on the alpha subunit. (**a**) cleft CM2 near helix H9 (shown in green ribbons); (**b**) cleft CM1 near helix H10 (shown in green ribbons), at the top of the dimer. The ligand shown in purple is Methoxyflurane, as extracted from a snapshot of the simulation with isotype αβVI. Rendering includes molecular surface in transparency, with lipophilic areas shown in green and hydrophilic areas shown in blue. Labels indicate nearby residues forming the cleft.

The second cleft, which corresponds to cleft CM1 shown in Figure 5B, is a nearby, mostly lipophilic patch located at the top of the alpha subunit and formed by helix H10 at the top and delimited by sheet S9 at the bottom

The broader picture of the binding patterns highlights how contact probabilities for each residue change with different ligands (ANOVA $p<0.0001$ for all three isotypes), more specifically pointing towards a clearly weaker interaction of Ethylene with all three isotypes, with mean contact probabilities significantly lower than the other three anesthetics (Dunnett's multiple comparisons test: $p<0.0001$ for all isotypes and ligands, except αβIIa with Halothane vs. Ethylene $p=0.0015$), and a global contact probability peak of 0.27 only with isotype αβIIa. Ethylene also showed a substantially lower predicted binding energy, coherently with the previous finding. Also, Methoxyflurane shows the most ubiquitous interactions with high overall contact probabilities during the simulation, peaking at 0.48 with αASN329 on isotype αβIVa, located in cleft CM1 (also visible as a darker area in Figure 3). Desflurane and Halothane show similar interaction patterns, both in terms of locations and probabilities, consistent with interactions in sterically compatible lipophilic patches located around the dimer. Notably, some interaction occurs on the side of the dimer facing the MT lumen (corresponding to the lower part of the graphs in Figures 3, 4 and 6 where $\varphi<<0$), especially on isotype αβIVa with methoxyflurane. Whether the MT lumen remains actually accessible to these ligands when the MT is assembled requires further investigations, but given the dimensions of these anesthetics, this appears to be feasible.

3.3.3 Protein-Ligand interaction energies

Binding energies for each anesthetic were predicted using the MM/PBSA method implemented in AmberTools, separately for each of the clefts reported in Table 3. Overall, predicted binding energies for Desflurane ranged from -7.10 ± 3.58 kcal/mol (isotype αβVI, cleft C_D1) to -14.89 ± 6.83 kcal/mol (isotype αβVI, cleft C_D4). In the case of Halothane, energies ranged from -6.31 ± 3.16 kcal/mol (isotype αβIIa, cleft C_H1) to -12.91 ± 3.17 kcal/mol (isotype αβIVa, cleft C_H3). Methoxyflurane featured binding energies from -7.13 ± 3.80 kcal/mol (isotype αβVI, cleft C_M1) to -14.55 ± 4.39 kcal/mol (isotype αβIIa, cleft C_M2). Lastly, in comparison, the predicted energies of Ethylene ranged from a minimum of -4.43 ± 0.97 kcal/mol (isotype αβIVa, cleft C_E1) to a maximum of -6.72± 1.74 kcal/mol (isotype αβIIa, cleft C_E1). The detailed map containing only the interaction clefts for all four ligands on isotype αβIVa is reported in Figure 6, where color intensity represents the predicted binding energy. The latter are also reported for all clefts and all ligands in Figure 7 as means with standard deviations. The decomposition of binding energies into VDWAALS, EEL, ENPOLAR and EDISPER components is reported for isotype αβIVa in Supplementary Figure S8 and shows the relative contribution of each term to the overall calculated binding energy, separately for each anesthetic and each binding site.

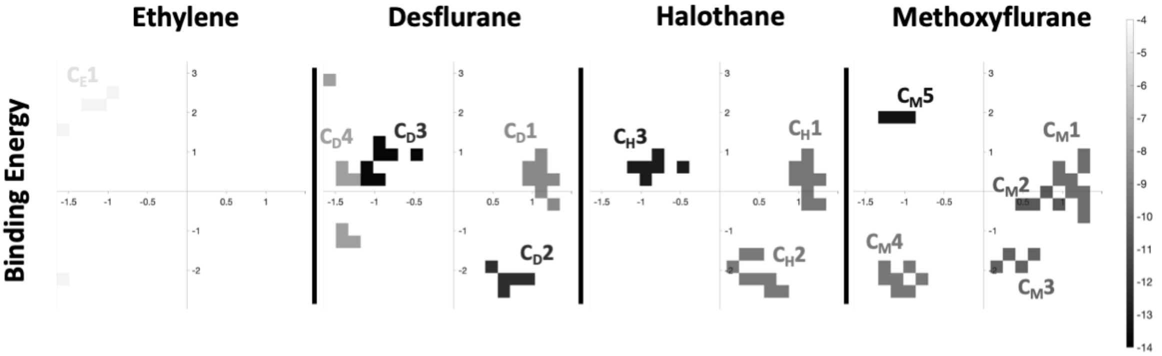

Figure 6. Per-area MM/PBSA binding energy estimate for isotype αβIVa, the one with the most overall interactions, with all the tested ligands. Left to right: Ethylene; Desflurane; Halothane; Methoxyflurane. Color scale is -4 kcal/mol to -14 kcal/mol. The different clefts are highlighted in the figure.

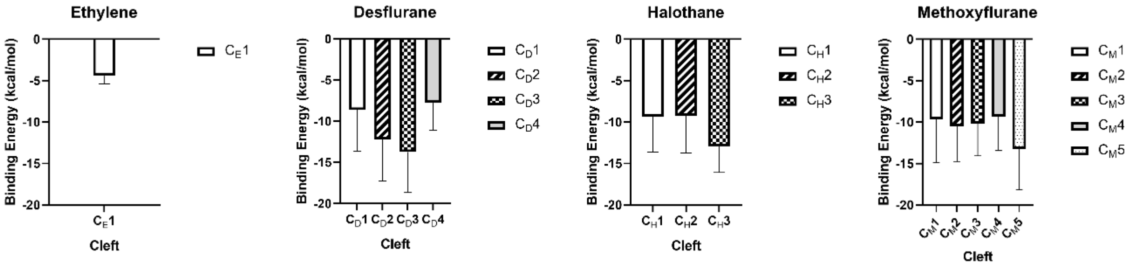

Figure 7. MM/PBSA binding energy estimates for isotype αβIVa with all the simulated ligands. Left to right: Ethylene; Desflurane; Halothane; Methoxyflurane. Data reported as mean with standard deviation bars for all clefts determined for each ligand.

Rather than representing definitive estimations for binding affinities, the collected data do however allow for a quantitative comparison between clefts and between different ligands, and show how the predicted binding energy is dependent of the specific surface cleft the ligand interacts with; the energy ranges and standard deviations yielded by MM/PBSA calculations are explainable with the transient nature of surface contacts inside the reported clefts, which do not allow, in the time scales investigated in the present work, for the formation of a protein-ligand complex which remains stable throughout the simulation. Rather, local alterations of sidechain arrangements permit the temporary accommodation of dissolved ligand in specific clefts, with average residence times as reported below. Interestingly, while all anesthetics tend to preferentially sample specific locations of the dimer surface, as discussed in the contact probability analysis and shown in figures 4, 5 and S7, the actual clefts where they eventually accommodate into are not always exactly the same, as detailed in Table 3 and visible in figure 6. In the case of isotype αβIVa, all ligands interact in the same cleft C1, whereas cleft C2 is largely the same for Desflurane and Halothane, but slightly shifted for Methoxyflurane, where it corresponds to cleft C3. The latter also featured three additional clefts C2 (near C1), C4 and C5 where no consistent binding emerged for the other anesthetics. Desflurane also showed a specific binding cleft, C4, located at the bottom of subunit beta towards the polymerization interface. This data confirms at the same time both the consistency of some binding sites, able to accommodate different ligands, and the existence of interaction areas which are selective towards some of the anesthetics. Also, as visible in Figures 6 and 7, Ethylene consistently showed the weakest predicted binding energy – and with lowest standard deviation – and the existence of only one weak binding site, in line with the previous contact probability analysis highlighting only negligible interaction.

3.3.4 Residence Times

Residence times were generally consistent with the reported contact probabilities: on isotype αβVI, Desflurane (Figure S22A) showed residence times in high-probability contact areas between 8 and 25 ns. Interestingly, the area with highest reported contact probability featured at the same time short average residence times, which is indicative of frequent short contacts, as opposed to stable binding. Halothane (Figure S22D) featured residence times between 3 and 25 ns near highly interacting residues, again with the area of peak probability showing frequent contacts of 7.5 ns on average. Methoxyflurane (Figure S22G) consistently showed average residence times between 6 and 24 ns near residues with high reported contact probabilities, most of them being above 15 ns where contact probability was the highest. As for the previous ligands, it showed an area on the alpha chain with frequent and short contacts (between 2 and 7 ns on average), as seen by the high reported per-residue contact probabilities, up to 0.37. Ethylene on the other hand (Figure S22L) featured residence times consistently below 5 ns, in good agreement with the low reported contact probabilities. On isotype αβIIa the average residence times of Desflurane (Figure S22B) spanned from 5 to 12 ns in areas with high contact probability. Again, high-probability contact residues on the alpha chain featured short mean residence times, below 10 ns, despite contact probabilities up to 0.35. Residence times for Halothane (Figure S22E) were between 7 and 22 ns on average around highly interacting residues, with the same area of short contacts below 10 ns on the alpha chain, with contact probabilities up to 0.22. Methoxyflurane (Figure S22H) featured the highest mean residence times, up to 23 ns and consistently above 12 ns in areas with high contact probability of up to 0.41. Ethylene (Figure S22M) confirmed the short residence times seen in the previous isotype, below 7 ns in most of the interacting residues, and with a maximum below 8 ns in the area with the highest contact probability (0.27). Lastly on isotype αβIVa, Desflurane (Figure S22C) interaction lasted on average up to 25 ns on chain alpha, and spanning from 4 to 19 ns in most other areas with high contact probability. Interestingly, the residue group with highest contact probability (0.56) also showed low average residence times, below 5 ns, indicative again of frequent short contacts, i.e. lower stability inside the cleft. Halothane (Figure S22F) residence times were higher on average, between 10 and 25 ns in most interaction areas. Also, contact probability peaks correspond to higher average residence times in all cases except one, near β295ASP, where a contact probability of 0.48 corresponded to mean residence times of 12 ns. In the case of Methoxyflurane (Figure S22I), areas with high contact probability corresponded to average residence times of the ligand between 4 and 25 ns, while the highest-probability cleft interacted on average for 14 ns. Finally, average residence times of ethylene (Figure S22N) never topped 5 ns, in agreement with the comparably low contact probability (0.21 at most). Interestingly, most areas with high contact probability showed particularly low residence times, below 1 ns, indicative of the lack of stable binding clefts.

3.3.5 Conformational Analysis

The RMSF analysis in the presence and absence of anesthetic molecules, respectively, focused on differences in C-alpha backbone fluctuations, for each of the three dimers. It is reported in detail in the Supplementary Information. Overall, different isotypes show slightly different behaviors in the presence of different anesthetics: The β M loop was destabilized on isotype αβVI with Desflurane and Methoxyflurane, while it showed decreased mobility in isotype αβIIa with Halothane, Methoxyflurane and Ethylene and in isotype αβIVa with halothane. A visible increase in fluctuations is reported in the area of residues 235-245 on the beta chain of isotype αβIIa in the presence of Methoxyflurane and Desflurane. The same isotype showed a similar spike in RMSF around residue 320 in the presence of Desflurane and Ethylene. Isotype αβIVa showed increased fluctuations on the β subunit at residues 325 to 340 with anesthetics compared to the control condition, which was not evident for the αβVI and αβIIa dimers. Overall, no major conformational changes were observed over the course of the simulations: cluster analysis of the trajectories, performed with a 0.15 nm cutoff, both with and without anesthetics, yielded a single dominant conformation for each run. In terms of secondary structure, possible alterations were assessed quantitatively using DSSP, comparing the secondary structure in the control simulations with the secondary structure in the ligand-bound state, separately for each binding site. As shown in Figure 8 for isotype αβIVa, no significant secondary structure alteration emerges throughout the dimer upon ligand binding in the different clefts. Differential interaction with different anesthetics might thus not be directly related to major conformational changes of the tubulin dimer.

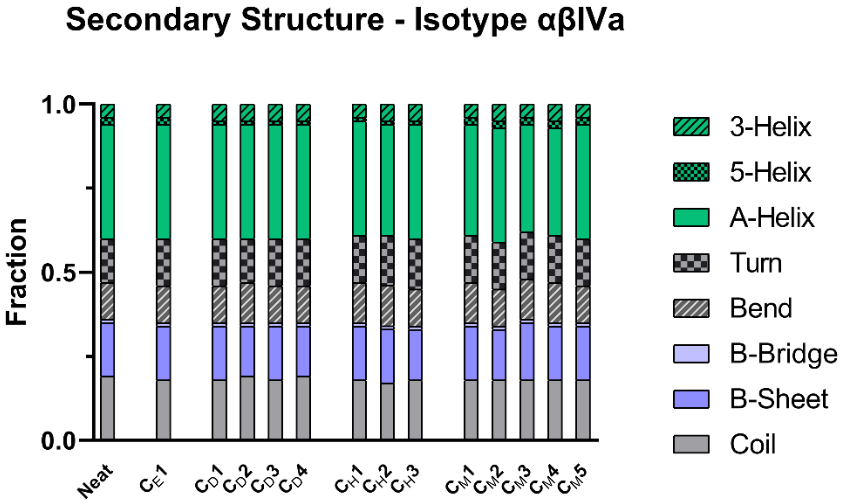

Figure 8. DSSP average Secondary Structure of the dimer in the control simulation without any ligands (“Neat”) vs. in the ligand-bound states, differentiated between different binding clefts. No significant alterations emerge.

4. Discussion

Blind docking of anesthetics to tubulin dimers αβVI, αβIIa and αβIVa highlighted low binding affinities compatible with a combination of hydrophobic interactions with surrounding residues. What emerges is a substantially indistinguishable predicted affinity between Halothane and Methoxyflurane, at a thermal noise level of k_BT, while affinity of Desflurane was predicted to be minimally better with respect to all three isotypes. What is consistently predicted is a much weaker affinity of Ethylene to all three isotypes, barely completing docking runs successfully and averaging at around -2.00 kcal/mol in every run. The important hint provided by blind docking experiments points toward the lack of a precise binding site, rather a preference for specific hydrophobic pockets of the tubulin dimers, able to transiently accommodate the anesthetic molecules. This underlined the weakness of the docking approach alone in the case of weak binders which interact at multiple sites simultaneously, and warranted a more thorough investigation of the interaction, in its dynamic nature, by simulating the dimer in the presence of anesthetic agents in the surrounding medium at fixed concentration.

Analysis of residue groups on the dimer surface with high probability of contact with each anesthetic confirmed that the tested compounds do not seem to have a single, specific binding site on the target, but they do, however, stay in contact with the dimer for prolonged times in specific clefts. These areas are partially overlapping for all isotypes and all tested VAs, with the notable exception of Ethylene, the weakest among the four, which showed a tendency to remain floating in the solvent rather than sticking to the dimer surface. The transient residence of volatile anesthetics may alter local mobility of residue sidechains with functional consequences on the MT, especially in the light of the high amount of predicted contact both in the luminal and lateral side of the tubulin dimers, where adjacent protofilaments assemble, as well as on the dimer-dimer polymerization interface. Contact probability, directly correlated to residence time at specific locations, confirmed similar interactions of Desflurane and Halothane, and a slightly increased interaction of Methoxyflurane with all isotypes. Moreover, the significantly weaker interactions of Ethylene emerged, consistent both with blind docking affinity estimates and with clinical potencies. Above all, the existence of different binding clefts, some of which shared between different anesthetics, some specific to a particular ligand, was confirmed. MM/PBSA predicted binding energies that were comparable, within error, between Desflurane, Halothane and Methoxyflurane, but again visibly lower for Ethylene, in agreement with the much lower contact probability.

Most notably, the three VAs Desflurane, Halothane and Methoxyflurane interacted in all the simulations of all three isotypes on the upper portion of the alpha subunit, predominantly in two lipophilic patches located near helices H9 and H10, an area corresponding in spherical coordinates to values of φ close to 0 and θ between 0.75 and 1.25. The patch around H9 is located on the lateral PF-PF contact area of the dimer, and might alter PF assembly in the presence of ligands, while the lipophilic pocket at helix H10, at the top of subunit alpha, might have functional consequences on tubulin polymerization in the process of dimer-dimer assembly. Ethylene did not show any interaction within these pockets.

Contact probability heatmaps also hint at how some high probability interaction zones were located near tryptophan residues, especially in the case of Halothane and Methoxyflurane on the alpha subunit in the area where αTRP21 is localized, i.e. $0.7<\theta<1.1$ and $0<\varphi<1$ in the spherical coordinate system (Supplementary Figure S7). The quantitative assessment of the involvement of Tryptophans in the interaction with anesthetic molecules requires further, more detailed work, possibly with higher-resolution methodologies. A direct role of tryptophan residues in the analyzed binding clefts was not confirmed with the methodologies used in the present work.

The interaction between volatile anesthetics and tubulin has been evaluated synergistically both through blind docking and Molecular Dynamics. The former approach confirmed the weak and transitory nature of putative binding sites suggested by previous research [54], by failing to highlight a single specific region of interaction and consistently reporting low predicted affinities across the different binding pockets. This consideration, along with the known limitations of blind docking [74], and the lack of single, high-affinity binding site following the more traditional lock-and-key paradigm for the investigated ligands, justified a more in depth analysis of the interaction through the use of molecular dynamics. In this last approach, the three different $\alpha\beta$-tubulin dimers have been simulated in the presence of a fixed concentration of anesthetics in the surrounding medium. To account for the dynamic nature of the interaction, *hotspots* of interaction have been determined on the dimer by sampling the contact probability between tubulin and anesthetic molecules on different portions of the dimer surface. Subsequently, precise binding clefts were determined from the contact map for further binding energy estimation. First, this clearly showed that interaction does feature preferential areas on the dimer surface and does not occur randomly. Rather, it appears to be driven mostly by the lipophilicity of the tested VAs. Secondly, it highlighted differences in interaction mostly between different anesthetics rather than between different tubulin isotypes: a given anesthetic tends to interact with specific areas of the dimer for tens of nanoseconds, and interaction may occur in close proximity of key functional residues of the microtubule. The areas of interaction were reproduced consistently, although with different residence times, in the different replicas, despite the low affinity of VAs for tubulin and the lack of a single, high-affinity binding site. There is no predicted preference of the simulated anesthetic agents for a specific tubulin isotype. More interestingly, a consistent amount of interaction is predicted to occur on the luminal surface of the assembled microtubule. Whether this area is accessible to volatile anesthetics and under which conditions, along with the functional and structural consequences of this on the microtubule structure, warrants further computational and experimental research. Since larger molecules, such as paclitaxel or epothilone, are known to bind on the luminal surface of microtubules due to the diffusion through the nanopores formed between neighboring tubulin dimers, a similar ability to reach the microtubule lumen appears entirely possible.

5. Conclusions

The present work computationally investigated the interaction between four distinct Volatile Anesthetics with different clinical potencies with human tubulin dimers, through Molecular Docking and Molecular Dynamics. The simulated isotypes are highly homologous, but each features a unique distribution across different organs and tissues, and the interaction of VAs with each of them appeared to be similar, but not identical. Results confirmed the absence of a lock-and-key type of interaction, and highlighted transient interactions on specific hotspots of the tubulin dimer, i.e. hydrophobic patches able to transiently accommodate the ligands. Methoxyflurane, the most potent among the tested VAs, showed the highest contact probability on all three simulated isotypes, while Ethylene, the weakest VA, had the lowest predicted binding affinity in Docking, the lowest overall contact probability in molecular dynamics simulations, and the lowest predicted binding energy in MM/PBSA calculations. These findings are consistent with previous works exploring the weak interaction between tubulin and anesthetics [9,24,29,75,76]. No distinct preference for a specific isotype emerges, while different anesthetics did show different interaction hotspots on the dimer surface, with only partial overlaps between them, the most notable of which is composed of two hydrophobic patches at the top of the alpha subunit, which interacted with all VAs except ethylene for a significant fraction of the simulations. Whether VAs can actually disrupt or alter microtubule assembly and dynamics, and how this process may occur, demands further investigations. While this process may not be directly involved in the primary mode of action of General Anesthetics, several considerations underline the importance of possible VA-tubulin interactions in the clinical context, including the abundance and peculiar anisotropic spatial organization of tubulin and microtubules in the brain; the role of microtubules in disorders such as POCD; putative cross-interactions with MT-targeting chemotherapies in oncological patients; side-effects in the presence of neurodegenerative diseases involving an altered MT cytoskeleton. In this context, effects of anesthetics could be of significance in the clinical setting and are worth exploring further.

6. Acknowledgements

We acknowledge the CINECA award under the ISCRA initiative, for the availability of high-performance computing resources and support.

Author Contributions: EAZ carried out the docking and molecular dynamics simulations and the subsequent analyses, interpreted and rationalized the results and wrote the paper. MD and JAT designed the study, interpreted the results and proof-read the paper. MC provided supervision about general anesthetics and their properties and clinical caveats, and interpreted the results.

Data Availability: All data supporting the findings of the study are available from the corresponding author, JAT, upon reasonable request.

Funding: This research received no external funding.

Conflicts of Interest: The authors declare no conflict of interest.

References

1. Craddock, T.J.A.; Kurian, P.; Preto, J.; Sahu, K.; Hameroff, S.R.; Klobukowski, M.; Tuszynski, J.A. Anesthetic Alterations of Collective Terahertz Oscillations in Tubulin Correlate with Clinical Potency: Implications for Anesthetic Action and Post-Operative Cognitive Dysfunction. *Sci. Rep.* **2017**, *7*, doi:10.1038/s41598-017-09992-7.

2. Meyer, H. Welche Eigenschaft der Anaesthetica bedingt ihre narkotische Wirkung? *Naunyn-Schmiedeberg's Arch Exp Pathol Pharmakol* **1899**, *42*, 109–118.

3. Meyer, H. Zur Theorie der Alkoholnarkose: 3. Mittheilung; der Einfluss wechselnder Temperatur auf Wirkungsstärke und Theilungscoefficient der Narcotica 1899.

4. Overton, C.E. Studien über die Narkose zugleich ein Beitrag zur allgemeinen Pharmakologie 1901.

5. Fütterer, C.D.; Maurer, M.H.; Schmitt, A.; Feldmann, R.E.; Kuschinsky, W.; Waschke, K.F. Alterations in Rat Brain Proteins after Desflurane Anesthesia. *Anesthesiology* **2004**, doi:10.1097/00000542-200402000-00019.

6. Pan, J.Z.; Xi, J.; Eckenhoff, M.F.; Eckenhoff, R.G. Inhaled anesthetics elicit region-specific changes in protein expression in mammalian brain. *Proteomics* **2008**, *8*, 2983–2992, doi:10.1002/pmic.200800057.

7. Kalenka, A.; Feldmann, R.E.; Kuschinsky, W.; Waschke, K.F.; Maurer, M.H. The Effects of Sevoflurane Anesthesia on Rat Brain Proteins : A Proteomic Time-Course Analysis. **2007**, *104*, 1129–1135, doi:10.1213/01.ane.0000260799.37107.e6.

8. Hameroff, S.; Penrose, R. Consciousness in the universe: A review of the "Orch OR" theory. *Phys. Life Rev.* 2014.

9. Tobias, J.W.; Eckenhoff, M.F.; Xi, J.; Eckenhoff, R.G.; Pan, J.Z. Halothane Binding Proteome in Human Brain Cortex. *J. Proteome Res.* **2006**, *6*, 582–592, doi:10.1021/pr060311u.

10. Avidan, M.S.; Evers, A.S. Review of clinical evidence for persistent cognitive decline or incident dementia attributable to surgery or general anesthesia. *J. Alzheimer's Dis.* 2011.

11. Monk, T.G.; Weldon, B.C.; Garvan, C.W.; Dede, D.E.; Van Der Aa, M.T.; Heilman, K.M.; Gravenstein, J.S. Predictors of cognitive dysfunction after major noncardiac surgery. *Anesthesiology* **2008**, doi:10.1097/01.anes.0000296071.19434.1e.

12. Lømo, T. The discovery of long-term potentiation. *Philos. Trans. R. Soc. B Biol. Sci.* 2003.

13. Bliss, T.V.P.; Collingridge, G.L.; Morris, R.G.M. Long-term potentiation: Enhancing neuroscience for 30 years - Introduction. *Philos. Trans. R. Soc. B Biol. Sci.* 2003.

14. Clugnet, M.C.; LeDoux, J.E. Synaptic plasticity in fear conditioning circuits: Induction of LTP in the lateral nucleus of the amygdala by stimulation of the medial geniculate body. *J. Neurosci.* **1990**, doi:10.1523/jneurosci.10-08-02818.1990.

15. Craddock, T.J.A.; Tuszynski, J.A.; Hameroff, S. Cytoskeletal signaling: Is memory encoded in microtubule lattices by CaMKII phosphorylation? *PLoS Comput. Biol.* **2012**, *8*, doi:10.1371/journal.pcbi.1002421.

16. Conde, C.; Cáceres, A. Microtubule assembly, organization and dynamics in axons and dendrites. *Nat. Rev. Neurosci.* **2009**, *10*, 319–332, doi:10.1038/nrn2631.

17. Kapitein, L.C.; Hoogenraad, C.C. Building the Neuronal Microtubule Cytoskeleton. *Neuron* **2015**, *87*, 492–506, doi:10.1016/j.neuron.2015.05.046.

18. Hameroff, S.; Nip, A.; Porter, M.; Tuszynski, J. Conduction pathways in microtubules, biological quantum computation, and consciousness. *Biosystems.* **2002**, *64*, 149–168.

19. HAMEROFF, S.R.; CRADDOCK, T.J.A.; TUSZYNSKI, J.A. "MEMORY BYTES" — MOLECULAR MATCH FOR CaMKII PHOSPHORYLATION ENCODING OF MICROTUBULE LATTICES . *J. Integr. Neurosci.* **2010**, *09*, 253–267, doi:10.1142/s0219635210002482.

20. Craddock, T.J.A.; Friesen, D.; Mane, J.; Hameroff, S.; Tuszynski, J.A. The feasibility of coherent energy transfer in microtubules. *J. R. Soc. Interface* **2014**, *11*, 2–10, doi:10.1098/rsif.2014.0677.

21. Tang, J.; Eckenhoff, M.F.; Eckenhoff, R.G. Anesthesia and the old brain. *Anesth. Analg.* **2010**, doi:10.1213/ANE.0b013e3181b80939.

22. Fodale, V.; Ritchie, K.; Rasmussen, L.S.; Mandal, P.K. Anesthetics and Alzheimer's disease: Background and research. *J. Alzheimer's Dis.* 2010.

23. Bowdle, T.A.; Knutsen, L.J.S.; Williams, M. Local and Adjunct Anesthesia. In *Comprehensive Medicinal Chemistry II*; Elsevier, 2007; pp. 351–367.

24. Livingston, A.; Vergara, G.A. Effects of halothane on microtubules in the sciatic nerve of the rat. *Cell Tissue Res.* **1979**, doi:10.1007/BF00234841.

25. Telser, A. The inhibition of flagellar regeneration in Chlamydomonas reinhardii by inhalational anesthetic halothane. *Exp. Cell Res.* **1977**, doi:10.1016/0014-4827(77)90406-2.

26. Riazi, S.; Ibarra Moreno, C.A. *Pharmacology and Physiology for Anesthesia*; Elsevier, 2013; Vol. 129; ISBN 9781437716795.

27. Mazze, R.I. Renal Dysfunction Associated With Methoxyflurane Anesthesia. *JAMA* **1971**, *216*, 278, doi:10.1001/jama.1971.03180280032006.

28. Porter, K.M.; Dayan, A.D.; Dickerson, S.; Middleton, P.M. The role of inhaled methoxyflurane in acute pain management. *Open Access Emerg. Med.* **2018**, *Volume 10*, 149–164, doi:10.2147/OAEM.S181222.

29. Hinkley, R.E. Microtubule—macrotubule transformations induced by volatile anesthetics. Mechanism of macrotubule assembly. *J. Ultrastruct. Res.* **1976**, *57*, 237–250, doi:10.1016/S0022-5320(76)80113-X.

30. Miller, R.D.; Wahrenbrock, E.A.; Schroeder, C.F.; Knipstein, T.W.; Eger, E.I.; Buechel, D.R. Ethylene--halothane anesthesia: addition or synergism? *Anesthesiology* **1969**, doi:10.1097/00000542-196910000-00002.

31. Bernardi, R.C.; Melo, M.C.R.; Schulten, K. Enhanced sampling techniques in molecular dynamics simulations of biological systems. *Biochim. Biophys. Acta* **2015**, *1850*, 872–877, doi:10.1016/j.bbagen.2014.10.019.

32. Lu, D.; Aksimentiev, A.; Shih, A.Y.; Cruz-Chu, E.; Freddolino, P.L.; Arkhipov, A.; Schulten, K. The role of molecular modeling in bionanotechnology. *Phys. Biol.* **2006**, *3*, S40--53, doi:10.1088/1478-3975/3/1/S05.

33. Hollingsworth, S.A.; Dror, R.O. Molecular Dynamics Simulation for All. *Neuron* **2018**, *99*, 1129–1143, doi:10.1016/j.neuron.2018.08.011.

34. Grasso, G.; Deriu, M.A.; Tuszynski, J.A.; Gallo, D.; Morbiducci, U.; Danani, A. Conformational fluctuations of the AXH monomer of Ataxin-1. *Proteins Struct. Funct. Bioinforma.* **2016**, *84*, 52–59, doi:10.1002/prot.24954.

35. Grasso, G.; Deriu, M.A.; Prat, M.; Rimondini, L.; Vernè, E.; Follenzi, A.; Danani, A. Cell Penetrating Peptide Adsorption on Magnetite and Silica Surfaces: A Computational Investigation. *J. Phys. Chem. B* **2015**, *119*, 8239–8246, doi:10.1021/jp512782e.

36. Apicella, A.; Soncini, M.; Deriu, M.A.; Natalello, A.; Bonanomi, M.; Dellasega, D.; Tortora, P.; Regonesi, M.E.; Casari, C.S. A Hydrophobic Gold Surface Triggers Misfolding and Aggregation of the Amyloidogenic Josephin Domain in Monomeric Form, While Leaving the Oligomers Unaffected. *PLoS One* **2013**, *8*, doi:10.1371/journal.pone.0058794.

37. Grasso, G.; Muscat, S.; Rebella, M.; Morbiducci, U.; Audenino, A.; Danani, A.; Deriu, M.A.M.A. Cell penetrating peptide modulation of membrane biomechanics by Molecular dynamics. *J. Biomech.* **2018**, *73*, 137–144, doi:10.1016/j.jbiomech.2018.03.036.

38. Deriu, M.A.M.A.; Grasso, G.; Licandro, G.; Danani, A.; Gallo, D.; Tuszynski, J.A.J.A.; Morbiducci, U. Investigation of the Josephin Domain Protein-Protein Interaction by Molecular Dynamics. *PLoS One* **2014**, *9*, e108677, doi:10.1371/journal.pone.0108677.

39. Huzil, J.T.; Ludueña, R.F.; Tuszynski, J. Comparative modelling of human $β$ tubulin isotypes and implications for drug binding. *Nanotechnology* **2006**, *17*, S90--S100, doi:10.1088/0957-4484/17/4/014.

40. Carpenter, E.J.; Huzil, J.T.; Ludueña, R.F.; Tuszynski, J. a Homology modeling of tubulin: influence predictions for microtubule's biophysical properties. *Eur. Biophys. J.* **2006**, *36*, 35–43, doi:10.1007/s00249-006-0088-0.

41. Leandro-García, L.J.; Leskelä, S.; Landa, I.; Montero-Conde, C.; López-Jiménez, E.; Letón, R.; Cascón, A.; Robledo, M.; Rodríguez-Antona, C. Tumoral and tissue-specific expression of the major human β-

tubulin isotypes. *Cytoskeleton* **2010**, *67*, 214–223, doi:10.1002/cm.20436.

42. Alushin, G.M.; Lander, G.C.; Kellogg, E.H.; Zhang, R.; Baker, D.; Nogales, E. High-resolution microtubule structures reveal the structural transitions in $α$$β$-tubulin upon GTP hydrolysis. *Cell* **2014**, *157*, 1117–1129, doi:10.1016/j.cell.2014.03.053.

43. Pettersen, E.F.; Goddard, T.D.; Huang, C.C.; Couch, G.S.; Greenblatt, D.M.; Meng, E.C.; Ferrin, T.E. UCSF Chimera?A visualization system for exploratory research and analysis. *J. Comput. Chem.* **2004**, *25*, 1605–1612, doi:10.1002/jcc.20084.

44. Martì-Renom, M.A.; Stuart, A.C.; Roberto, S.; Melo, F.; Andrej, S. COMPARATIVE PROTEIN STRUCTURE MODELING OF GENES AND GENOMES. *Annu. Rev. Biophys. Biomol. Struct* **2000**, *29*, 291–325.

45. Laskowski, R.A.; MacArthur, M.W.; Moss, D.S.; Thornton, J.M. PROCHECK: a program to check the stereochemical quality of protein structures. *J. Appl. Crystallogr.* **1993**, *26*, 283–291, doi:10.1107/S0021889892009944.

46. Hooft RW; Vriend G; Sander C; Abola EE Errors in Protein structures. *Nature* **1996**, *381*, 272.

47. Colovos, C.; Yeates, T.O. Verification of protein structures: patterns of nonbonded atomic interactions. *Protein Sci.* **1993**, *2*, 1511–1519, doi:10.1002/pro.5560020916.

48. Eisenberg, D.; Lüthy, R.; Bowie, J.U. VERIFY3D: Assessment of protein models with three-dimensional profiles. *Methods Enzymol.* **1997**, *277*, 396–404.

49. Benkert, P.; Tosatto, S.C.E.; Schomburg, D. QMEAN: A comprehensive scoring function for model quality assessment. *Proteins Struct. Funct. Genet.* **2008**, *71*, 261–277, doi:10.1002/prot.21715.

50. Benkert, P.; Biasini, M.; Schwede, T. Toward the estimation of the absolute quality of individual protein structure models. *Bioinformatics* **2011**, *27*, 343–350, doi:10.1093/bioinformatics/btq662.

51. Waterhouse, A.; Bertoni, M.; Bienert, S.; Studer, G.; Tauriello, G.; Gumienny, R.; Heer, F.T.; De Beer, T.A.P.; Rempfer, C.; Bordoli, L.; et al. SWISS-MODEL: Homology modelling of protein structures and complexes. *Nucleic Acids Res.* **2018**, *46*, W296–W303, doi:10.1093/nar/gky427.

52. Morris, G.M.; Huey, R.; Lindstrom, W.; Sanner, M.F.; Belew, R.K.; Goodsell, D.S.; Olson, A.J. AutoDock4 and AutoDockTools4: Automated Dockingwith Selective Receptor Flexibility. *J. Comput. Chem.* **2009**, *30*, 2786–2791.

53. Trott, O.; Olson, A.J. Software News and UpdateAutoDock Vina: Improving the Speed and Accuracy ofDocking with a New Scoring Function, EfficientOptimization, and Multithreading. *J. Comput. Chem.* **2010**, *31*, 455–461, doi:10.1002/jcc.21334.

54. Craddock, T.J.A.; George, M.; Freedman, H.; Barakat, K.H.; Damaraju, S.; Hameroff, S.; Tuszynski, J.A. Computational predictions of volatile anesthetic interactions with the microtubule cytoskeleton: Implications for side effects of general anesthesia. *PLoS One* **2012**, *7*, doi:10.1371/journal.pone.0037251.

55. Chau, P.L. New insights into the molecular mechanisms of general anaesthetics. *Br. J. Pharmacol.* **2010**, *161*, 288–307, doi:10.1111/j.1476-5381.2010.00891.x.

56. Guo, J.; Zhou, C.; Liang, P.; Huang, H.; Li, F.; Chen, X.; Liu, J. Comparison of subarachnoid anesthetic effect of emulsified volatile anesthetics in rats. *Int. J. Clin. Exp. Pathol.* **2014**, *7*, 8748–8755.

57. Humphrey, W.; Dalke, A.; Schulten, K. VMD: visual molecular dynamics. *J. Mol. Graph.* **1996**, *14*, 27-28,33-38, doi:10.1016/0263-7855(96)00018-5.

58. Abraham, M.J.; Murtola, T.; Schulz, R.; Páll, S.; Smith, J.C.; Hess, B.; Lindahl, E. GROMACS: High performance molecular simulations through multi-level parallelism from laptops to supercomputers. *SoftwareX* **2015**, *1–2*, 19–25, doi:10.1016/j.softx.2015.06.001.

59. Lindorff-Larsen, K.; Piana, S.; Palmo, K.; Maragakis, P.; Klepeis, J.L.; Dror, R.O.; Shaw, D.E. Improved side-chain torsion potentials for the Amber ff99SB protein force field. *Proteins* **2010**, *78*, 1950–1958, doi:10.1002/prot.22711.

60. Wishart, D.S. DrugBank: a comprehensive resource for in silico drug discovery and exploration. *Nucleic Acids Res.* **2006**, *34*, D668–D672, doi:10.1093/nar/gkj067.

61. Wang, J.; Wang, W.; Kollman, P.A.; Case, D.A. Automatic atom type and bond type perception in molecular mechanical calculations. *J. Mol. Graph. Model.* **2006**, *25*, 247–260, doi:10.1016/j.jmgm.2005.12.005.

62. Jakalian, A.; Jack, D.B.; Bayly, C.I. Fast, efficient generation of high-quality atomic charges. AM1-BCC model: II. Parameterization and validation. *J. Comput. Chem.* **2002**, *23*, 1623–1641, doi:10.1002/jcc.10128.

63. Berendsen, H.J.C.J.C.; Postma, J.P.M.; Van Gunsteren, W.F.; DiNola, A.; Haak, J.R. Molecular dynamics with coupling to an external bath. *J. Chem. Phys.* **1984**, *81*, 3684–3690, doi:10.1063/1.448118.

64. Parrinello, M.; Rahman, A. Polymorphic transitions in single crystals: A new molecular dynamics method. *J. Appl. Phys.* **1981**, *52*, 7182–7190, doi:10.1063/1.328693.

65. Ewald, P. Die Berechnung optischer und elektrostatischer Gitterpotentiale. *Ann. Phys.* **1921**.

66. Touw, W.G.; Baakman, C.; Black, J.; te Beek, T.A.H.; Krieger, E.; Joosten, R.P.; Vriend, G. A series of PDB-related databanks for everyday needs. *Nucleic Acids Res.* **2015**, *43*, D364–D368, doi:10.1093/nar/gku1028.

67. Nogales, E.; Wolf, S.G.; Downing, K.H. Structure of the ab tubulin dimer by electron crystallography. *Nature* **1998**, *391*, 199–204.

68. Gowers, R.; Linke, M.; Barnoud, J.; Reddy, T.; Melo, M.; Seyler, S.; Domański, J.; Dotson, D.; Buchoux, S.; Kenney, I.; et al. MDAnalysis: A Python Package for the Rapid Analysis of Molecular Dynamics Simulations. *Proc. 15th Python Sci. Conf.* **2016**, 98–105, doi:10.25080/majora-629e541a-00e.

69. Naveen, M.-A.; Denning, E.J.; Woolf, T.B.; Beckstein, O. MDAnalysis: A toolkit for the analysis of molecular dynamics simulations. *J. Comput. Chem.* **2011**, *32*, doi:https://doi.org/10.1002/jcc.21787.

70. Kollman, P.A.; Massova, I.; Reyes, C.; Kuhn, B.; Huo, S.; Chong, L.; Lee, M.; Lee, T.; Duan, Y.; Wang, W.; et al. Calculating structures and free energies of complex molecules: combining molecular mechanics and continuum models. *Acc. Chem. Res.* **2000**, *33*, 889–897.

71. Case, D.A.; Belfon, K.; Ben-Shalom, I.Y.; Brozell, S.R.; Cerutti, D.S.; Cheatham, T.E.I.; Cruzeiro, V.W.D.; Darden, T.A.; Duke, R.E.; Giambasu, G.; et al. AMBER 2020 2020.

72. Molecular Operating Environment (MOE) 2019.01 2019.

73. Webb, B.; Sali, A. Comparative Protein Structure Modeling Using MODELLER. *Curr. Protoc. Bioinforma.* **2016**, *54*, 5.6.1-5.6.37, doi:https://doi.org/10.1002/cpbi.3.

74. Pantsar, T.; Poso, A. Binding Affinity via Docking: Fact and Fiction. *Molecules* **2018**, *23*, 1–11, doi:10.3390/molecules23081899.

75. Eckenhoff, R.G.; Johansson, J.S. Molecular interactions between inhaled anesthetics and proteins. *Pharmacol. Rev.* **1997**, *49*, 343–367.

76. Sahni, P. Tubulin Conformation and Anaesthetic Interaction - An Experimental Study. *Biochem. Anal. Biochem.* **2016**, *s3*, 1–7, doi:10.4172/2161-1009.1000251.